










OPEN

# Experimental observation of open structures in elemental magnesium at terapascal pressures

M. G. Gorman<sup>1,2</sup>  , S. Elatresh<sup>3,4</sup>, A. Lazicki<sup>1</sup> , M. M. E. Cormier<sup>1,5</sup> , S. A. Bonev<sup>1</sup>, D. McGonegle<sup>6,7</sup>, R. Briggs<sup>1,2</sup>, A. L. Coleman<sup>1,2</sup>, S. D. Rothman<sup>7</sup>, L. Peacock<sup>7</sup>, J. V. Bernier<sup>1</sup>, F. Coppari<sup>1</sup> , D. G. Braun<sup>1</sup>, J. R. Rygg<sup>8</sup>, D. E. Fratanduono<sup>1</sup>, R. Hoffmann<sup>3</sup>, G. W. Collins<sup>8</sup>, J. S. Wark<sup>6</sup> , R. F. Smith<sup>1</sup>, J. H. Eggert<sup>1</sup>  and M. I. McMahon<sup>2</sup>

**Investigating how solid matter behaves at enormous pressures, such as those found in the deep interiors of giant planets, is a great experimental challenge. Over the past decade, computational predictions have revealed that compression to terapascal pressures may bring about counter-intuitive changes in the structure and bonding of solids as quantum mechanical forces grow in influence<sup>1–6</sup>. Although this behaviour has been observed at modest pressures in the highly compressible light alkali metals<sup>7,8</sup>, it has not been established whether it is commonplace among high-pressure solids more broadly. We used shaped laser pulses at the National Ignition Facility to compress elemental Mg up to 1.3 TPa, which is approximately four times the pressure at the Earth's core. By directly probing the crystal structure using nanosecond-duration X-ray diffraction, we found that Mg changes its crystal structure several times with non-close-packed phases emerging at the highest pressures. Our results demonstrate that phase transformations of extremely condensed matter, previously only accessible through theoretical calculations, can now be experimentally explored.**


At extreme compressions, found in the cores of large rocky exoplanets, it was traditionally believed that solid matter would assemble in close-packed, metallic crystal structures with such stability that structural rearrangements would be highly unlikely<sup>9,10</sup>. However, the advent of modern computational tools for predicting structures and electronic properties at any arbitrary volume has suggested a new paradigm for a wide range of highly compressed materials<sup>1–6</sup>. Calculations for matter at terapascal pressures indicate that solid materials may adopt non-close-packed lattice arrangements to accommodate clouds of localized valence electrons forced away from the core electrons by Coulombic interactions and Pauli exclusion<sup>11</sup>. Theory predicts that the structure of elemental Mg will transform multiple times at pressures approaching 1 TPa as the influence of these quantum effects grows. Close-packed structures such as hexagonal close-packed (hcp) and face-centred cubic (fcc), which are stable in Mg at ambient and moderate pressures, are predicted to be replaced with hexagonal and cubic structures containing more interstitial space within the lattice<sup>1,2,4,5</sup>. Similar behaviour has been observed in the light alkali metals at more modest pressures due

to their high compressibility and low electronegativity<sup>7,8</sup>. It remains unknown whether such behaviour is ubiquitous in high-pressure solids, as terapascal pressures are inaccessible using standard experimental techniques: such pressures are incredibly challenging to achieve at present using static compression methods<sup>12</sup> and sample heating associated with shock compression precludes the study of solid matter at 1 TPa.

To reach the terapascal regime to study solid Mg, we used the National Ignition Facility (NIF) and directly probed the crystal structure at peak pressure with nanosecond-duration X-ray diffraction. Our experiments reveal four new, distinct, non-close-packed structures of Mg at 0.31 TPa, 0.56 TPa, 0.96 TPa and 1.32 TPa. Diffraction at the highest pressures is consistent with the formation of simple hexagonal and simple cubic phases in agreement with decade-old computational predictions<sup>4,5</sup>. These results represent the observation of solid–solid phase transformations occurring at terapascal pressures and offer experimental insights into how pressure-induced quantum effects can drive structural stability at extreme conditions.

We used 16 beams of the NIF to launch an ablatively driven uniaxial-compression wave into a Mg sample (see Methods). The ramp-shaped laser pulse allowed the sample to achieve high compression at cool enough temperatures to remain in the solid state. Pressure in the sample gradually increased over the 25 ns duration of the laser pulse, before pressure uniformity was achieved for several nanoseconds at peak compression. The target package consisted of a 50- $\mu\text{m}$ -thick polycrystalline Mg foil sandwiched between a Be anvil, coated with a thin Au preheat shield, and a diamond window (Supplementary Fig. 1 and Extended Data Table 1). This target assembly was placed at the front of the target diffraction in situ (TARDIS) diagnostic (Fig. 1)<sup>13</sup>. A Ge backlighter foil, positioned near the front surface of the TARDIS, was irradiated by 24 beams of the NIF for 2 ns to produce quasi-monochromatic He  $\alpha$  radiation (characteristic X-ray wavelength of 1.209 Å)<sup>14</sup>. The X-ray pulse was timed to probe the sample once it had achieved a uniform pressure state. Diffraction patterns were collected in a transmission geometry on X-ray sensitive image plates placed on the inside top, bottom and rear surfaces of the TARDIS box. Figure 1 shows a representative diffraction pattern in stereographic projection such that

<sup>1</sup>Lawrence Livermore National Laboratory, Livermore, CA, USA. <sup>2</sup>SUPA, School of Physics & Astronomy and Centre for Science at Extreme Conditions, The University of Edinburgh, Edinburgh, UK. <sup>3</sup>Department of Chemistry and Chemical Biology, Cornell University, Baker Laboratory, Ithaca, NY, USA.

<sup>4</sup>Physics Department, King Fahd University of Petroleum and Minerals, Dhahran, Saudi Arabia. <sup>5</sup>Department of Physics & Atmospheric Science, Dalhousie University, Halifax, Nova Scotia, Canada. <sup>6</sup>Department of Physics, Clarendon Laboratory University of Oxford, Oxford, UK. <sup>7</sup>Atomic Weapons Establishment, Reading, UK. <sup>8</sup>Departments of Mechanical Engineering, Physics and Astronomy and Laboratory for Laser Energetics, University of Rochester, Rochester, NY, USA.  e-mail: [gorman11@lln.gov](mailto:gorman11@lln.gov)

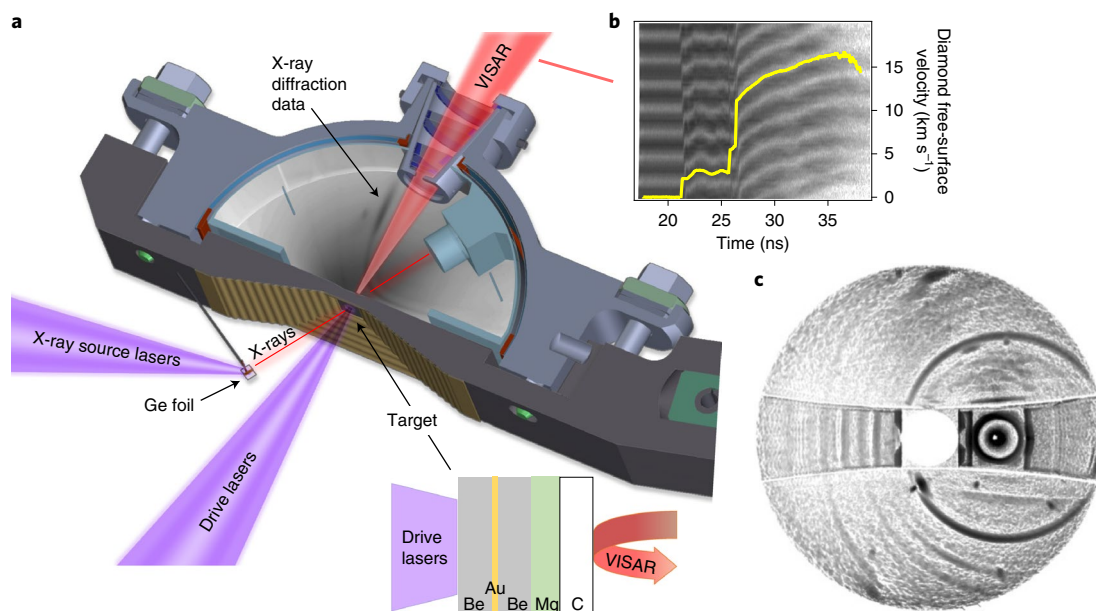


**Fig. 1 | Experimental set-up of the terapascal NIF diffraction experiments.** **a**, The Mg sample is situated at the front of the TARDIS box, where it is compressed by a temporally shaped laser pulse. A typical target assembly is shown. Laser irradiation of a Ge foil generates an  $\sim 10.2$  keV X-ray source that probes the sample at peak compression. The diffraction pattern is collected on X-ray sensitive image plates situated within the TARDIS diagnostic. **b**, Representative free-surface velocity history (yellow line) as measured by the velocity interferometry system for any reflector (VISAR) in each experiment. **c**, A stereographic projection of a representative diffraction data collected at 0.41 TPa.

the Debye–Scherrer diffraction rings appear as concentric circles. The rear surface velocity of the diamond tamper was measured in each experiment using the velocity interferometry system for any reflector diagnostic<sup>15</sup>, which determines the sample pressure history<sup>13</sup> using the known equation of state of diamond<sup>16,17</sup>. Sample temperatures were not measured in these experiments but were estimated to range from 2,500 K at 0.31 TPa to 5,000 K at 1.32 TPa using radiation-coupled hydrodynamic simulations (Supplementary Information).

We observed four distinct phases of Mg up to 1.32 TPa. Figure 2a displays four representative diffraction images collected at 0.31 TPa, 0.56 TPa, 0.96 TPa and 1.32 TPa, projected such that the Debye–Scherrer diffraction rings appear as vertical lines of constant scattering angle. The azimuthally averaged one-dimensional (1D) profiles for all experiments are shown in Fig. 2b, with the diffraction peaks from compressed Mg shaded. In some experiments, non-sample diffraction peaks were observed either from the Be pusher, Au heat shield or single-crystal diamond window (Extended Data Figs. 1–6). Six diffraction reflections from the compressed Mg sample were visible at 0.31 TPa (Fig. 2b). From an analysis of the location of these reflections, it is clear that the body-centred cubic (bcc) phase that is predicted to be stable at these conditions cannot explain all observed reflections. However, the diffraction data are consistent with a bcc-like structure, given that the location of the strongest reflections are similar to those predicted for bcc phases, in addition to the observation of weaker diffraction peaks (Fig. 3a). We propose a structural candidate, a bc6 structure, that explains all reflections and gives a reasonable density (Supplementary Fig. 2), but this structure was calculated to have considerably higher enthalpy than the bcc phase. We are therefore unable to unambiguously determine the structure of this phase. A similar diffraction pattern, suggestive of a similar structure, was also collected at 0.41 TPa (Fig. 2b and Extended Data Fig. 6).

At 0.56 TPa, five diffraction reflections from the Mg sample were observed (Fig. 2b). The fcc phase that is predicted to be stable at these conditions could not explain all observed reflections<sup>5</sup>. However, as before, diffraction peaks in similar locations to those predicted for

fcc, as well as the observation of several weak reflections, pointed towards the actual structure being a distortion of fcc. We found that a structure with space group symmetry  $Fmmm$  and four atoms in the conventional unit cell ( $Z=4$ ) explained all observed reflections (Fig. 3a) and was energetically competitive with fcc (Supplementary Fig. 7). This new phase of Mg is an orthorhombic distortion of fcc with the main structural changes involving an  $\sim 11\%$  contraction of the  $a$  lattice parameter and an  $\sim 15\%$  expansion of the  $c$  lattice parameter with little relative change to the  $b$  axis. The measured lattice parameters are  $a=2.58(1)$  Å,  $b=2.91(1)$  Å and  $c=3.35(1)$  Å where the numbers in parenthesis represent  $1\sigma$  uncertainties.

At 0.96 TPa, two diffraction peaks from the Mg sample were observed. Although we are unable to unambiguously determine the structure from these data, the diffraction is consistent with the simple hexagonal structure (space group symmetry  $P6/mmm$  ( $Z=1$ )), predicted to be the stable structure at these conditions<sup>5</sup>. Assuming a simple hexagonal structure, the measured  $c/a$  ratio ( $c/a=0.87(1)$ ) agrees well with the prediction from previous density functional theory (DFT) calculations ( $c/a=0.90$ )<sup>3,5</sup> supporting our assignment of this phase. The measured lattice parameters are  $a=1.87(1)$  Å and  $c=1.63(1)$  Å. Furthermore, the  $d$  spacings of the two observed reflections were compared with DFT predictions for energetically favourable high-pressure phases (Fig. 3a and Supplementary Fig. 2) and shown to be consistent with only the simple hexagonal phase, within experimental uncertainty. Given the low signal-to-noise ratio of the diffraction data at 0.96 TPa, there may be other weak diffraction lines present that we were unable to resolve. However, as we saw no evidence of other diffraction lines, we chose to make the simplest interpretation of the data that was also supported by theoretical predictions<sup>5</sup>. One diffraction peak observed at 0.41 TPa, 0.56 TPa and 0.96 TPa is consistent with a bcc phase of Be, the material used as the pusher in these experiments (Fig. 3a, Supplementary Figs. 5 and 6 and Supplementary Table 1). This phase has been predicted to become stable above 0.3 TPa (refs. 18–21).

At 1.32 TPa, the observed diffraction pattern also showed two peaks. Again, while we were unable to definitively determine the structure of the Mg sample at these conditions, the two diffraction

peaks were consistent with the simple cubic structure (space group symmetry  $Pm\bar{3}m$  ( $Z=1$ )) predicted to be stable at these conditions<sup>5</sup>. Observed  $d$  spacings were again compared with DFT predictions for the candidate phases at 1.32 TPa (Fig. 3a and Supplementary Fig. 10), and only the simple cubic phase assignment is consistent within experimental uncertainty. As with the diffraction patterns collected at 0.96 TPa, we cannot rule out the presence of additional weak diffraction peaks in the data but chose the simplest interpretation of the data, which is that the sample forms the simple cubic structure, in agreement with theoretical predictions<sup>5</sup>. The simple cubic lattice parameter is  $a=1.60(1)$  Å. To our knowledge this is the highest-pressure structural phase transition observed and corresponds to an  $\sim 5.5$ -fold compression of Mg.

The measured pressures and densities of the assigned  $Fm\bar{3}m$ , simple hexagonal and simple cubic phases are compared with DFT predictions in Fig. 3b. The density for the phases observed at 0.31 TPa and 0.41 TPa was calculated assuming a bcc phase, using the reflections consistent with bcc, as a likely phase assignment was not found for the apparently distorted structure (see Extended Data Table 2 for more information on measured diffraction locations, densities and uncertainties). We investigated this unexpected observation of non-close-packed structures at 0.31 TPa, 0.41 TPa and 0.56 TPa (fcc was predicted to be stable to 0.76 TPa; ref.<sup>5</sup>) by performing structure searches at 0 K. We found several lower-symmetry phases (Supplementary Fig. 7) that are energetically competitive at these conditions. Among them is the orthorhombic  $Fm\bar{3}m$  phase observed experimentally, which lies within 20 meV of the stable fcc phase. This suggests that elevated temperatures present in the ramp-compressed Mg ( $\sim 4,200$  K predicted, see the Supplementary Information) may stabilize the  $Fm\bar{3}m$  phase—a surprising result, as symmetry-breaking transitions are commonly considered to be low-temperature phenomena<sup>22</sup>. However, phonon free-energy calculations within the quasi-harmonic approximation show that the  $Fm\bar{3}m$  phase of Mg has larger entropy ( $S$ ) than fcc such that at elevated temperatures, the Gibbs free energy ( $G=H-TS$ ), where  $T$  is temperature and  $H$  is enthalpy, of  $Fm\bar{3}m$  becomes lower than fcc (Supplementary Fig. 7). The  $Fm\bar{3}m$  phase was also found to be dynamically stable with no negative phonon frequencies (Supplementary Fig. 8).

The key finding of this study is the experimental observation that non-close-packed structures do become stable at terapascal pressures and over fivefold compression, confirming the predictions of theoretical calculations for Mg and other elemental systems over the past decade<sup>1,2,4,5</sup>. The drop in coordination number from 12 in ambient hcp Mg to 8 in the simple hexagonal phase at 0.96 TPa and 6 in the simple cubic phase at 1.32 TPa contradicts our traditional expectation that crystals should pack more efficiently with increasing compression<sup>9,10</sup>. However, similar predictions at terapascal pressures for several other elemental systems such as C (ref.<sup>3</sup>), Al (ref.<sup>4</sup>) and Si (ref.<sup>6</sup>) suggest that this behaviour could be relatively general. At extreme compression, as valence electron density is forced away from atomic sites due to Coulomb effects and Pauli exclusion, the system can be stabilized by forming electroneutral structures

in which charge is localized into interstitial sites in the lattice. Structures such as simple hexagonal and simple cubic, which are energetically unfavourable configurations at ambient conditions due to their low atomic packing fractions (60% for simple hexagonal and 52% for simple cubic), emerge as the most stable configurations at terapascal pressures as their larger interstitial regions

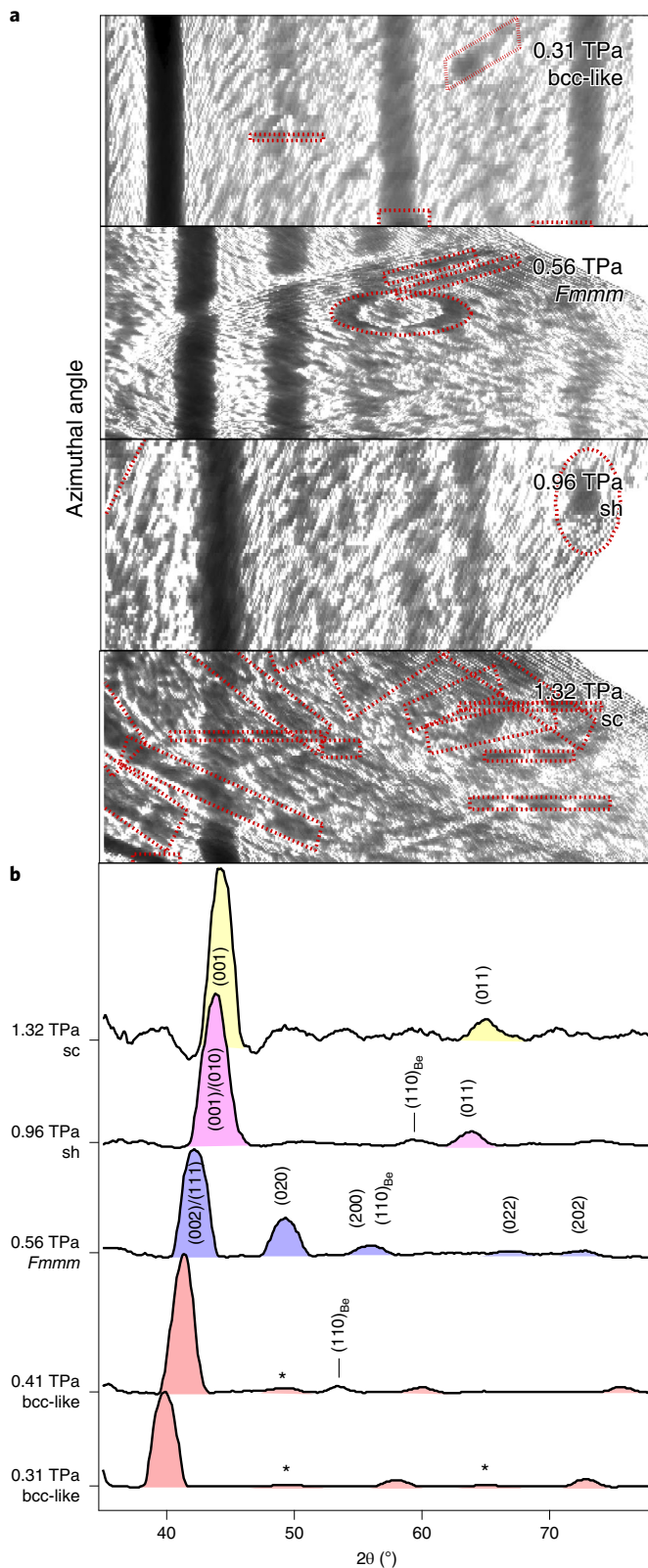


**Fig. 2 | X-ray diffraction from extremely compressed magnesium.**

**a**, Four representative 2D diffraction images collected at 0.31 TPa, 0.56 TPa, 0.96 TPa and 1.32 TPa (top to bottom) and projected into  $\phi$  (azimuthal angle)– $2\theta$  (diffraction angle) space. **b**, Corresponding azimuthally averaged diffraction data. Diffraction from the Mg sample is highlighted by shading and the Miller indices of the determined phases are labelled where possible. Non-sample, or non-diffraction features in the 2D image have been masked out for clarity (red dashed outlines in **a**). Weak reflections inconsistent with the bcc phase are highlighted in the 0.31 TPa and 0.41 TPa profiles with black asterisks. Diffraction peaks originating from the Be pusher are observed in some experiments and are also highlighted.

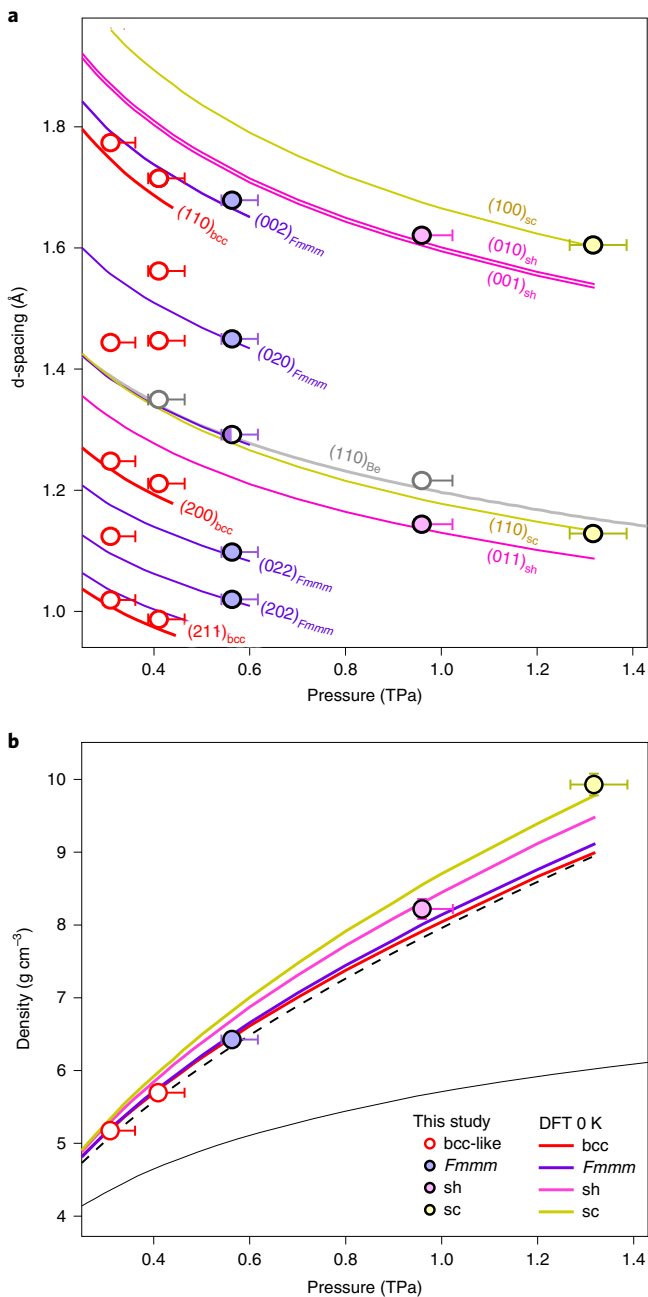


**Fig. 3 | Comparison with theoretical predictions.** **a**, Comparison of measured d spacings (circles) with density function theory (DFT) simulations conducted at zero temperature (0 K) for the bcc,  $Fm\bar{3}m$ , simple hexagonal and simple cubic phases of Mg and the bcc phase of Be (coloured lines). The simulated bcc lines are shown to highlight the similarities with some of the measured d spacings at 0.31 TPa and 0.41 TPa. One marker at 0.56 TPa is shaded grey/purple to indicate that the observed diffraction peak intensity had contributions from both the Mg sample and Be pusher. **b**, Calculated pressure–density relations for various phases of Mg with experimentally-determined values overlaid. An extrapolation of the PV relation of bcc Mg from 300 K static compression<sup>23</sup> (solid black line) and the PV relation for shock-compressed Mg from a tabular EOS (SESAME EoS 2860)<sup>24,25</sup> (dashed black line) are also shown for comparison. Error bars represent  $1\sigma$  uncertainties in pressure.

mean that they can accommodate localized charge density more easily than close-packed structures (74% atomic packing fraction) (Supplementary Fig. 7). In Fig. 4, we show calculations of the

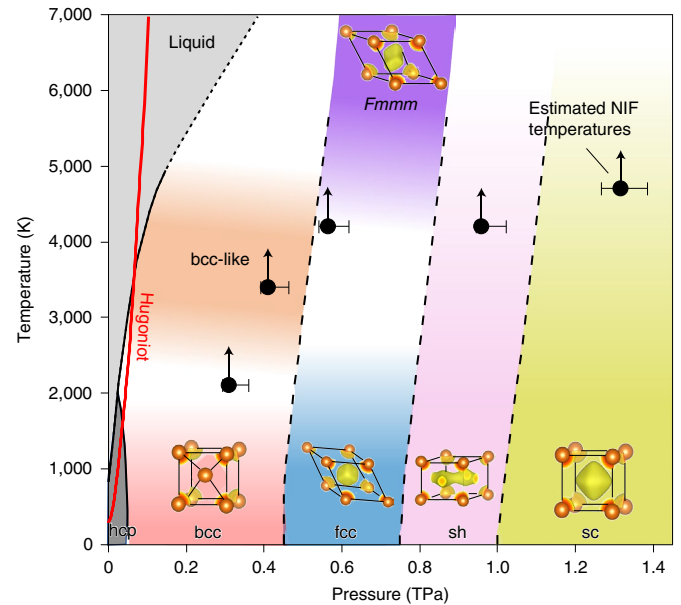


**Fig. 4 | Pressure–temperature phase diagram of Mg.** The phase diagram was constructed using static compression (solid black line)<sup>23</sup> and previous DFT calculations (dashed black lines)<sup>5</sup>. Black circles with upward arrows represent estimates of Mg temperatures for the NIF experiments based on hydrocode simulations that incorporate radiation coupling and thermal transport models (Supplementary Information). Error bars represent  $1\sigma$  uncertainties in pressure. The calculated Hugoniot is shown (red line). The primitive unit cells of the stable phases and the localized valence charge are shown (yellow regions) (conventional unit cell is shown for the bcc structure). High-temperature regions representing the bcc-like and  $Fm\bar{3}m$  regions are indicated.

electronic localization function for the observed and predicted structures of Mg (yellow regions in each unit cell) (see Methods). Our calculations, as well as previous studies<sup>4,5</sup>, predicted that valence charge accumulates in the interstitial regions of simple hexagonal Mg, centred at the  $2d$  ( $\frac{1}{3}, \frac{2}{3}, \frac{1}{2}$ ) Wyckoff site of the simple hexagonal lattice (Fig. 4) and the  $1b$  ( $\frac{1}{2}, \frac{1}{2}, \frac{1}{2}$ ) Wyckoff site of the simple cubic lattice (Fig. 4) forming pseudo-ionic  $MgE_2$  and  $MgE$  structures (where E denotes localized-electron pseudo-anions), analogous to the  $AlB_2$  and CsCl structures. We suggest that the direct observation of the simple hexagonal and simple cubic phases of Mg is experimental evidence of how core–valence and core–core electron interactions can influence material structure at terapascal pressures. Figure 4 shows our revised temperature–pressure phase diagram of Mg to 7,000 K and 1.4 TPa. Our experiments complement previous 0 K theoretical investigations and have mapped out high-temperature regions of the Mg phase space, discovering new distorted cubic structures between 0.31 TPa and 0.56 TPa, as well as the simple hexagonal and simple cubic structures at 0.96 TPa and 1.32 TPa.

Using X-ray diffraction, we report four new phases of Mg up to 1.32 TPa giving experimental insight into phase transformations in extremely compressed solids above 1 TPa. Our diffraction measurements show clear evidence of non-close-packed, open structures emerging as the most stable configurations at terapascal pressures, providing experimental evidence of the formation of novel electrified states and confirming decade-old predictions.

### Online content

Any methods, additional references, Nature Research reporting summaries, source data, extended data, supplementary information, acknowledgements, peer review information; details of

author contributions and competing interests; and statements of data and code availability are available at <https://doi.org/10.1038/s41567-022-01732-7>.

Received: 16 December 2021; Accepted: 15 July 2022;  
Published online: 19 September 2022

## References

1. Miao, M. S. & Hoffmann, R. High pressure electrides: a predictive chemical and physical theory. *Acc. Chem. Res.* **47**, 1311–1317 (2014).
2. Miao, M. S. & Hoffmann, R. High-pressure electrides: the chemical nature of interstitial quasiatoms. *Acc. Chem. Res.* **137**, 3631–3637 (2015).
3. Martinez-Canales, M., Pickard, C. J. & Needs, R. J. Thermodynamically stable phases of carbon at multiterapascal pressures. *Phys. Rev. Lett.* **108**, 45704 (2012).
4. Pickard, C. J. & Needs, R. J. Aluminium at terapascal pressures. *Nat. Mater.* **9**, 624–627 (2010).
5. Li, P., Gao, G., Wang, Y. & Ma, Y. Crystal structures and exotic behavior of magnesium under pressure. *J. Phys. Chem. C* **114**, 21745–21749 (2010).
6. Paul, R., Hu, S. X. & Karasiev, V. V. Anharmonic and anomalous trends in the high-pressure phase diagram of silicon. *Phys. Rev. Lett.* **122**, 125701 (2019).
7. Ma, Y. Transparent dense sodium. *Nature* **458**, 182–185 (2009).
8. Hanfland, M., Christensen, N. E. & Novikov, D. L. New high-pressure phases of lithium. *Nature* **408**, 174–178 (2000).
9. Prewitt, C. T. & Downs, R. T. High-pressure crystal chemistry. *Rev. Mineral.* **37**, 283 (1998).
10. Grochala, W., Hoffmann, R., Feng, J. & Ashcroft, N. W. The chemical imagination at work in very tight places. *Angew. Chem. Int. Ed.* **46**, 3620–3642 (2007).
11. Rousseau, B. & Ashcroft, N. W. Interstitial electronic localization. *Phys. Rev. Lett.* **101**, 046407 (2008).
12. Dubrovinskaia, N. et al. Terapascal static pressure generation with ultrahigh yield strength nanodiamond. *Sci. Adv.* **2**, 7 (2016).
13. Rygg, J. R. et al. X-ray diffraction at the National Ignition Facility. *Rev. Sci. Instrum.* **91**, 043902 (2020).
14. Coppar, F. Optimized x-ray sources for x-ray diffraction measurements at the Omega Laser Facility. *Revi. Sci. Instrum.* **90**, 125113 (2019).
15. Celliers, P. M. et al. Line-imaging velocimeter for shock diagnostics at the OMEGA laser facility. *Rev. Sci. Instrum.* **75**, 4916 (2004).
16. Bradley, D. K. et al. Diamond at 800 GPa. *Phys. Rev. Lett.* **102**, 75503 (2009).
17. Smith, R. F. et al. Ramp compression of diamond to five terapascals. *Nature* **511**, 330–333 (2014).
18. Benedict, L. X. et al. Calculations of high-pressure properties of beryllium: construction of a multiphase equation of state. *Phys. Rev. B* **79**, 064106 (2009).
19. Legrand, R. G. et al. Multiphase equation of state and elastic moduli of solid beryllium from first principles. *Phys. Rev. B* **82**, 10 (2010).
20. Luo, F. et al. Ab initio calculation of lattice dynamics and thermodynamic properties of beryllium. *J. App. Phys. A* **111**, 053503 (2012).
21. Wu, C. J. et al. Development of a multiphase beryllium equation of state and physics-based variations. *J. Phys. Chem. A* **125**, 1610–1636 (2021).
22. Chandrasekhar, S. *Liquid Crystals* (Cambridge Univ. Press, 1992).
23. Stinton, G. W. et al. Equation of state and high-pressure/high-temperature phase diagram of magnesium. *Phys. Rev. B* **90**, B03208 (2014).
24. Johnson, J. D. & Lyon, S. P. *SESAME: The Los Alamos National Laboratory Equation Of State Database* Technical Report No. LA-UR-92-3407 (Los Alamos National Laboratory, 1992).
25. Marsh, S. P. *LASL Shock Hugoniot Data* Vol. 5 (Univ. California Press, 1980).

**Publisher's note** Springer Nature remains neutral with regard to jurisdictional claims in published maps and institutional affiliations.



**Open Access** This article is licensed under a Creative Commons Attribution 4.0 International License, which permits use, sharing, adaptation, distribution and reproduction in any medium or format, as long as you give appropriate credit to the original author(s) and the source, provide a link to the Creative Commons license, and indicate if changes were made. The images or other third party material in this article are included in the article's Creative Commons license, unless indicated otherwise in a credit line to the material. If material is not included in the article's Creative Commons license and your intended use is not permitted by statutory regulation or exceeds the permitted use, you will need to obtain permission directly from the copyright holder. To view a copy of this license, visit <http://creativecommons.org/licenses/by/4.0/>.

© The Author(s) 2022

## Methods

**Experimental methods.** Experiments were performed at the NIF at the Lawrence Livermore National Laboratory. Targets consisted of a 50  $\mu\text{m}$  polycrystalline Mg foil, sandwiched between a 200  $\mu\text{m}$  diamond window and a 20  $\mu\text{m}$  Be pusher that was bonded to a 40  $\mu\text{m}$  Be ablator (Fig. 1). We used a double-sided non-contact ZYGO white-light interferometer to measure a 3D surface optical profile ( $x$ - $y$  spatial dimensions and  $z$  height relative to a reference measurement) of all parts before assembly and again during assembly after each subsequent epoxy layer was added, resulting in a thickness uncertainty of less than 0.2  $\mu\text{m}$  for each component. More details can be found in ref.<sup>13</sup>. Thin coatings of Re and Au were deposited between the pusher and ablator to protect the sample from X-ray heating from the drive plasma and the X-ray source. The target package was mounted onto a 400- $\mu\text{m}$ -diameter pinhole made of U + 6%Nb, which was positioned on the front of the TARDIS diagnostic (Fig. 1)<sup>13</sup>. After background subtraction<sup>13</sup>, the 2D diffraction images were azimuthally averaged to give 1D diffraction profiles. To perform the calibration of the system, geometry diffraction lines from a compressed sample were used as input features for an optimization routine as described in Rygg et al.<sup>13</sup>. Each diffraction line was constrained to have the same  $2\theta$  along a given Debye–Scherrer arc; this assumes that the effects of pressure non-uniformity, sample strength or finite grain size do not cause  $2\theta$  distortions of the diffraction lines. Samples were compressed using 16 beams of NIF with temporally shaped laser pulses of 25 ns duration and peak intensities up to  $1 \times 10^{14} \text{ W cm}^{-2}$ . The drive beams were incident  $40$ – $46^\circ$  from normal and 1 mm continuous phase plates were used to smooth the beam profile. The drive beams were pointed into four quadrants to achieve an  $\sim 1.8$  mm drive spot. This configuration has been demonstrated to achieve transverse uniformity in the drive sample<sup>13</sup>. A typical pulse shape used in these experiments is shown in Supplementary Fig. 11. Quasi-monochromatic X-rays were generated by irradiating a Ge foil with 24 beams of NIF with a 2 ns laser pulse with a peak intensity of  $2 \times 10^{15} \text{ W cm}^{-2}$ . The X-rays were emitted isotropically from the Ge foil. Diffracted X-rays from the Mg sample were collimated by the pinhole and collected on a set of X-ray sensitive image plates in the TARDIS diagnostic. Plastic and Ge filters were placed in front of the image plates to absorb unwanted X-rays. While we use the term ‘pressure’ throughout the manuscript, our samples were uniaxially compressed. The presence of deviatoric stress states (not measured) due to high-pressure strength could result in states that deviate from ideal hydrostaticity.

**Theoretical methods.** First-principles structure searches, enthalpy calculations and molecular dynamics simulations were performed with the Vienna ab initio simulation package (VASP)<sup>26</sup> within the Perdew–Burke–Ernzerhof generalized gradient approximation<sup>27</sup> of DFT. We used a ten electron projector augmented wave pseudopotential from the VASP library with an 800 eV plane wave cutoff and 1.7 Bohr outmost core radius. We performed first-principles molecular dynamics simulations of liquid Mg along the 10,000 K isotherm over the pressure range of interest. These were carried out with 128-atom supercells in the canonical (constant volume, temperature and particle number) ensemble, with the  $(\frac{1}{4}, \frac{1}{4}, \frac{1}{4})$  k-point sampling of the Brillouin zone, Fermi–Dirac smearing and a Nosé–Hoover thermostat with a 1 fs ionic time step. The liquid was quenched at pressures around 350 and 650 GPa until signs of solidification appeared. From the lowest temperature liquid ( $T \approx 5,000$  K) obtained at each pressure random configurations were taken with cluster sizes between 2 and 10 Å, for which full structural optimizations were carried out. These optimizations were carried out at (target) pressures of 0.32, 0.6 and 0.96 TPa. Overall, about 300, 400 and 100 configurations were generated and optimized at each of the three pressures, respectively, with the number of atoms ranging from 1 to 30. To confirm that this search procedure was exhaustive, we carried out additional genetic structure search and adaptive metadynamics calculations using the Universal Structure Predictor Evolutionary Xtallography (USPEX) package<sup>28–32</sup>. These were carried out with 20–30 hereditary generations, starting with 60 random structures with unit cells of 1 to 28 atoms, 50% of each generation were used to create the next, and k-point sampling with a reciprocal space resolution of 0.039. However, no additional competitive structures were found. The enthalpies of the most competitive structures within a 50 meV per atom window found by the liquid sampling method at 0.32, 0.6 and 0.96 TPa were then computed in the range from 0 to 1.3 TPa. For the final structural calculations and enthalpy computations, the Brillouin zone was sampled with dense k-point meshes sufficient to ensure enthalpy convergence better than 1 meV per atom ( $22 \times 22 \times 22$  for fcc and simple cubic,  $28 \times 28 \times 28$  for bcc and simple hexagonal,  $18 \times 18 \times 18$  for hcp,  $24 \times 24 \times 24$  for *Fmmm* (Supplementary Table 2),  $36 \times 36 \times 36$  for *Immm* and *R-3m*, and  $6 \times 6 \times 6$  for *Pnma*). The accuracy of the VASP pseudopotential in describing Mg at the highest pressure considered here was verified by carrying out additional calculations with the ABINIT code<sup>33</sup> and using a norm-conserving pseudopotential with a 1.56 Bohr outmost core radius and 1,360 eV cutoff. Finally, phonon and Gibbs free-energy calculations were performed within the DFT perturbation theory<sup>34</sup> as implemented in ABINIT. The dynamical matrices were computed on uniform  $5 \times 5 \times 5$  q-point meshes in the Brillouin zone, from which interatomic force constants were obtained and used to interpolate the phonon dispersions on  $38 \times 38 \times 38$  q-point meshes. As discussed in the main text, we found from first-principles theory that *Fmmm* trends towards stability over fcc Mg at very high temperature. However, we note that the energy

differences between fcc and *Fmmm* are relatively small and anharmonic effects are neglected in the quasi-harmonic Gibbs free-energy calculations, and therefore this method cannot be used to accurately predict the transition temperature, but instead only indicate the trend with increasing temperature. To quantify the degree of interstitial electron localization (yellow regions of unit cells in Fig. 4), we computed the electron localization function (ELF) from 0 K unit cells at selected pressures.  $\text{ELF} = 0.5$  corresponds to the electron gas (that is, delocalized electrons) and  $\text{ELF} = 1.0$  corresponds to perfect localization. We deemed  $\text{ELF} > 0.75$  to correspond to localized electrons. We then partitioned the charge density in regions where  $\text{ELF} > 0.75$  and  $\text{ELF} < 0.75$ . Integrating the interstitial region where  $\text{ELF} > 0.75$  gave the number of localized electrons. It is worth noting that absolute magnitudes depend on the choice of ELF cutoff, but the general trend is not very sensitive to this choice.

## Data availability

The data shown in Figs. 1–4 are available in Extended Data Tables 1 and 2. Additional data are available from the corresponding author upon request.

## Code availability

The data analysis code implementing the methods described in ref.<sup>13</sup> is publicly available at <https://github.com/HEXRD>.

## References

- Kresse, G. & Hafner, J. Ab initio molecular dynamics for liquid metals. *Phys. Rev. B* **47**, 558 (1993).
- Perdew, J. P., Burke, K. & Ernzerhof, M. Generalized gradient approximation made simple. *Phys. Rev. Lett.* **78**, 1396 (1997).
- Oganov, A. R. & Glass, C. W. Crystal structure prediction using ab initio evolutionary techniques: principles and applications. *J. Chem. Phys.* **124**, 244704 (2006).
- Oganov, A. R., Lyakhov, A. O. & Valle, M. How evolutionary crystal structure prediction works—and why. *Acc. Chem. Res.* **44**, 227–237 (2011).
- Lyakhov, A. O., Oganov, A. R., Stokes, H. T. & Zhu, Q. New developments in evolutionary structure prediction algorithm USPEX. *Comput. Phys. Commun.* **184**, 1172–1182 (2013).
- Zhu, Q., Oganov, A. R., Lyakhov, A. O. & Yu, X. Generalized evolutionary metadynamics for sampling the energy landscapes and its applications. *Phys. Rev. B* **92**, 024106 (2015).
- Zhu, Q., Oganov, A. R. & Lyakhov, A. O. Evolutionary metadynamics: a novel method to predict crystal structures. *CrystEngComm* **14**, 3596–3601 (2012).
- Gonze, X. et al. ABINIT: first-principles approach to material and nanosystem properties. *Comp. Phys. Commun.* **180**, 2582–2615 (2009).
- Gonze, X. & Lee, C. Dynamical matrices, Born effective charges, dielectric permittivity tensors, and interatomic force constants from density-functional perturbation theory. *Phys. Rev. B* **55**, 10337 (1997).
- Lazicki, A. et al. Metastability of diamond ramp-compressed to 2 terapascals. *Nature* **589**, 532–535 (2021).

## Acknowledgements

We thank the National Ignition Facility staff and the National Ignition Facility Discovery Science programme. This work was performed under the auspices of the US Department of Energy by Lawrence Livermore National Laboratory under contract number DE-AC52-07NA27344. J.S.W. thanks the UK EPSRC for support under grant numbers EP/J017256/1 and EP/S025065/1. M.I.M. thanks the UK EPSRC for support under grant numbers EP/J017051/1 and EP/R02927X/1. M.I.M. is grateful to AWE for the award of a William Penney Fellowship. D.M. was supported by LLNS under contract number B595954. Partial funding for G.W.C. and J.R.R. was provided by NSF Physics Frontier Center award number PHY-2020249 and DOE NNSA award number DE-NA0003856. Funding for this research was provided by the Center for Matter at Atomic Pressures (CMAP), a National Science Foundation (NSF) Physics Frontiers Center, under award number PHY-2020249 (to G.W.C., J.H.E. and J.R.R.). This material is based in part upon work supported by the Department of Energy, Office of Science, Fusion Energy Sciences under award number DE-SC0020340 (to A.L., M.I.M., J.H.E., G.W.C. and J.R.R.). S.E. thanks E. J. Nicol for research support and discussions.

## Author contributions

M.I.M. and J.H.E. conceived the work. M.G.G., A.L., D.M., J.R.R., R.F.S., A.L.C. and R.B. performed the experiments. S.E., S.A.B. and M.M.E.C. performed the first-principles calculations. D.G.B., S.D.R. and L.P. designed the laser pulse shapes. A.L., J.H.E. and M.G.G. analysed the data with assistance from J.V.B., J.R.R. and D.E.F. F.C., G.W.C., J.S.W. and R.H. contributed to the design of the work and interpretation of the data. M.G.G. wrote the paper. All co-authors commented critically on the manuscript.

## Competing interests

The authors declare no competing interests.

**Additional information**

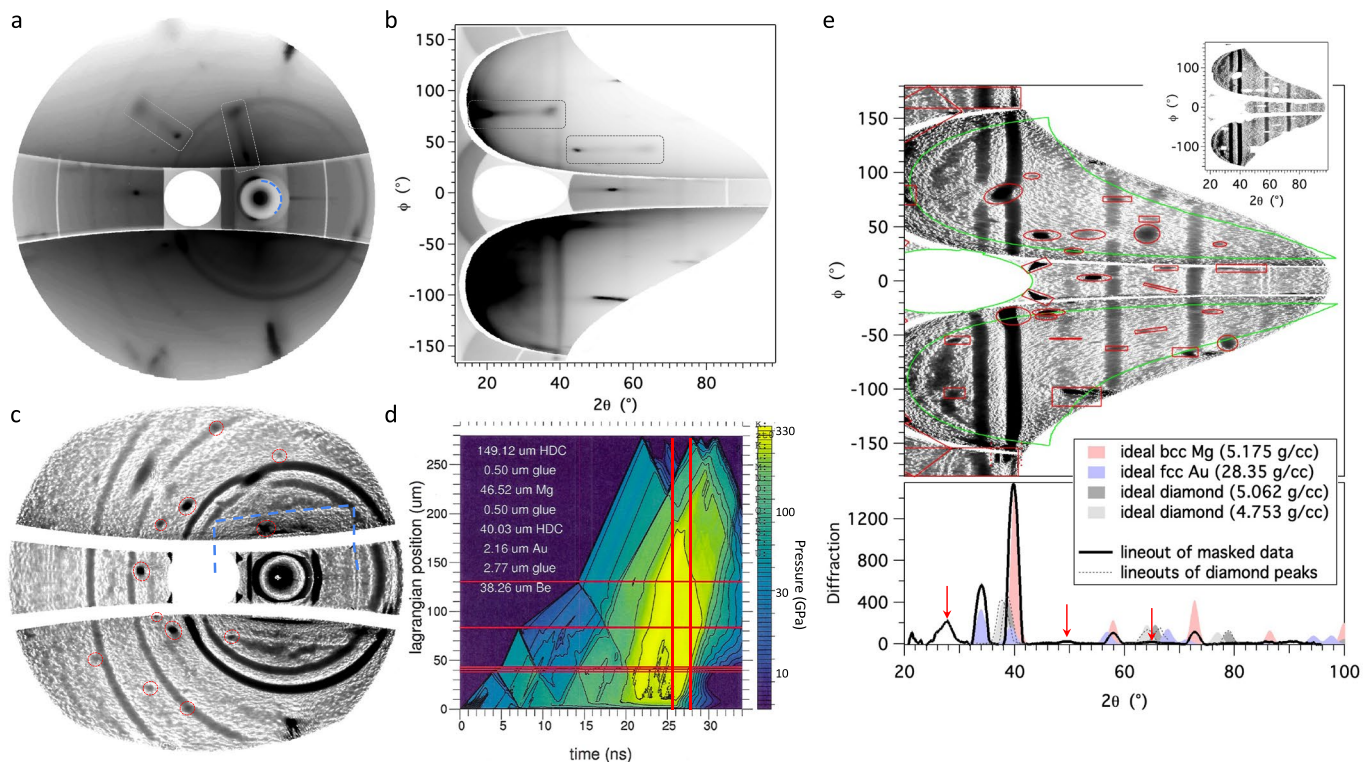
**Extended data** is available for this paper at <https://doi.org/10.1038/s41567-022-01732-7>.

**Supplementary information** The online version contains supplementary material available at <https://doi.org/10.1038/s41567-022-01732-7>.

**Correspondence and requests for materials** should be addressed to M. G. Gorman.

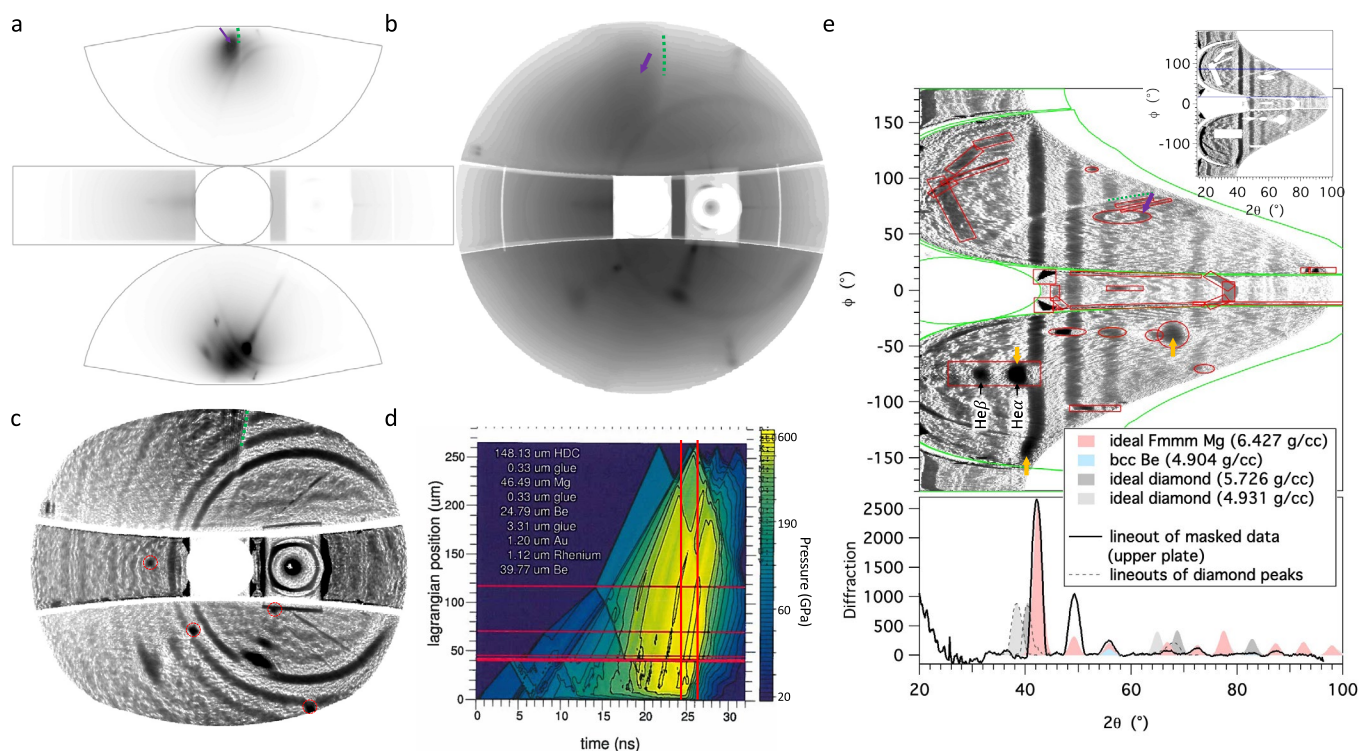
**Peer review information** *Nature Physics* thanks Yanming Ma and the other, anonymous, reviewer(s) for their contribution to the peer review of this work.

**Reprints and permissions information** is available at [www.nature.com/reprints](http://www.nature.com/reprints).

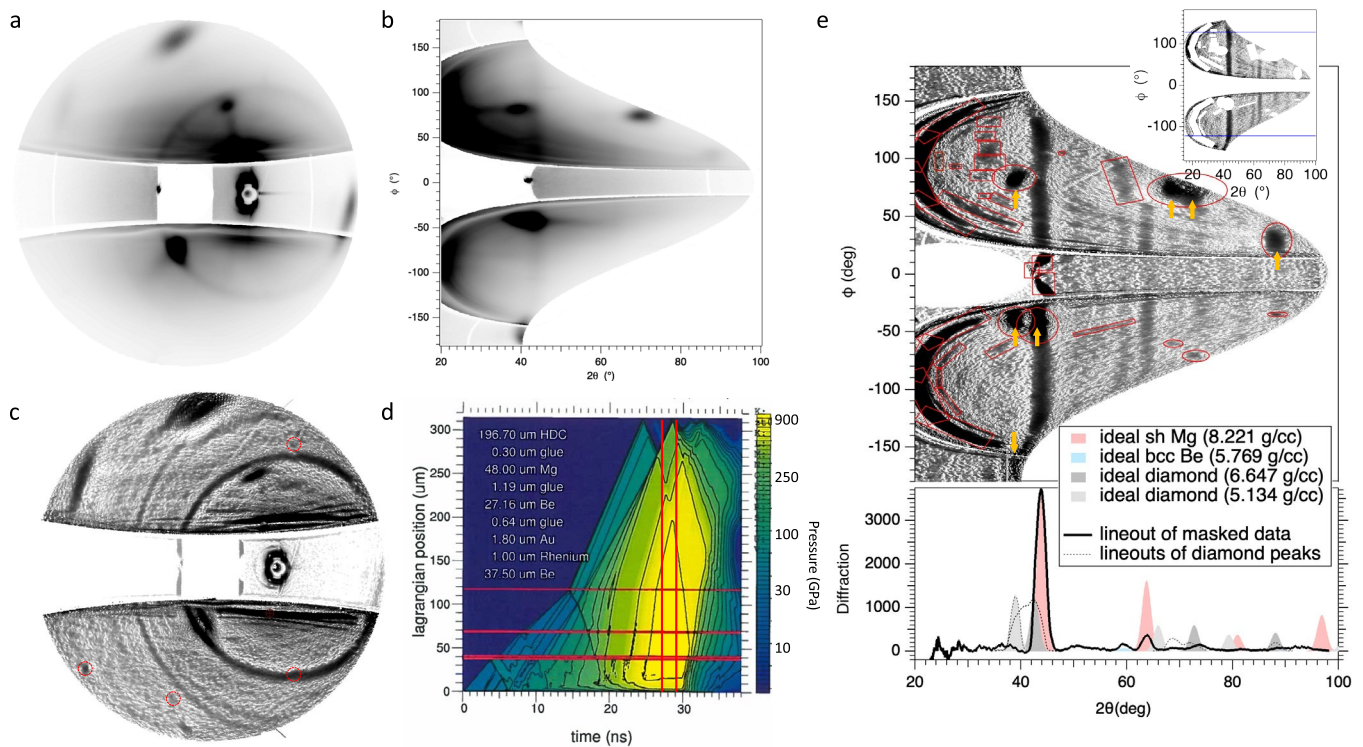


**Extended Data Fig. 1 | Summary of shot N170209-003 (0.31 TPa).** Raw image plate data are warped into stereographic (a) and polar (b) projections. Background-subtracted stereographic data is shown in (c) and (d) shows a radiation-hydrodynamic simulation of this experiment, with colors corresponding to pressure. The interfaces between different materials in the sample are indicated with horizontal red lines and the timing of the x-ray source is bracketed with vertical red lines. All materials in the sample (diamond, gold, and Mg) may scatter x-rays onto the image plates during the time between ~25.5 and 27.5 ns. (e) shows the background-subtracted polar projection. Everything within the red contours, which outline spurious features, and outside of the green contours, which encompass the region of interest on the image plates, is masked out to produce the image in the inset. An average lineout of the masked data (lower panel) is then analyzed to determine peak angles via peak-fitting, and the peak angles are used in a least-squares fitting to determine a density for each phase, assuming a structure consistent with the observed peaks. The ideal diffraction patterns shown in the lower panel of (e) are simulated from the structure factor, multiplicity, Lorentz-Polarization factor (for a flat powder sample in transmission), and an instrument broadening tuned to match the data. The relative intensities of the Au and Mg simulated data are determined based on the relative thicknesses and scattering factors of these two target layers. One factor not accounted for in the simulated diffraction, because we do not measure the temperature, is the Debye-Waller attenuation of the intensity of higher-angle diffraction peaks. The gold heat shield layer is especially hot (very close to melted), so we expect that high-angle lines which appear in the simulated pattern are likely not to show up above the background in the data. Several spurious features in the data are indicated in (a), (b) and (c): the Bragg diffraction rings are centered around the direct x-ray beam, which terminates in a high-Z cylindrical canister. The walls of the canister cast the circular shadow which is partially outlined with a blue dashed line in (a). The cylindrical canister is held in place within the TARDIS body by a square polycarbonate fixture, which also casts a shadow evident in (c) (partially outlined with a blue dashed line). The x-ray source has a broad bremsstrahlung component to the spectrum in addition to the quasi-monochromatic He-alpha x-rays, which scatter off of the single-crystal diamonds in the target package and are registered as Laue spots, marked with red circles in (c). For the strongest Laue spots, an elongated streak of weaker scattering, outlined with grey rectangular boxes in (a) and (b), can be seen out to much higher angle, due to the large variation in d-spacing present in the diamond window as a result of the strong pressure gradient (simulated in (d)). The compressed diamond also breaks up to some extent and scatters highly-textured Bragg peaks as well, indicated by the thin dashed lineouts in the lower panel of (e). The bulk of the diamond appears to be in two distinct states illustrated by the two ideal diamond diffraction patterns shown in grey in the lower panel of (e): diamond compressed to approximate pressure equilibrium with the sample in the pusher layer (illustrated in (d)), and in about 1/3 of the window layer closest to the Mg sample. About 1/4 of the window layer is released down to a slightly lower pressure, due to the release wave propagating back into the window after the diamond elastic wave reaches the free surface of the window at around 20 ns. The remainder of the diamond is undergoing a steep pressure gradient. Diffraction features that are not identified are indicated with red arrows in the lower panel of (e), suggesting a lower-symmetry bcc-like Mg structure. The lowest-angle peak near 28 degrees is potentially a background artifact, because it falls just adjacent to the shadow of the polycarbonate fixture illustrated with the blue dashed line in (c). The presence of the shadow on that region of the image plate means that any peaks at angles lower than about 30 degrees could be obscured, so they can't be definitively confirmed or ruled out. One other feature worth noting is an artifact of the background-subtraction: in the region just adjacent to a strong diffraction feature, the signal and background gets strongly attenuated in a halo around that feature. This is the reason that the otherwise very non-textured and powder-like diffraction peaks appear to have some cutouts on the upper image plate in (e). Those regions of signal attenuation are where the Bragg peak is overlapping with the streaked diamond Laue signal, or with the diamond Bragg scattering.

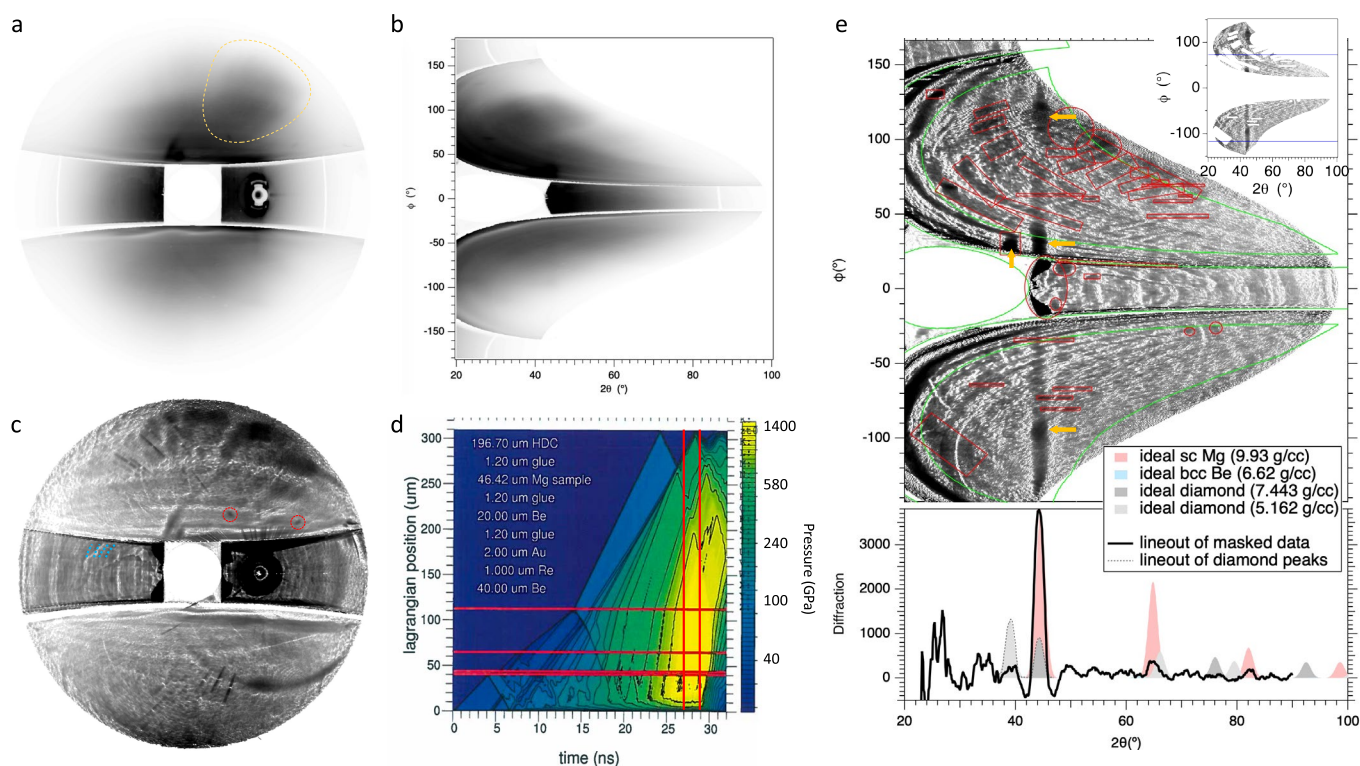




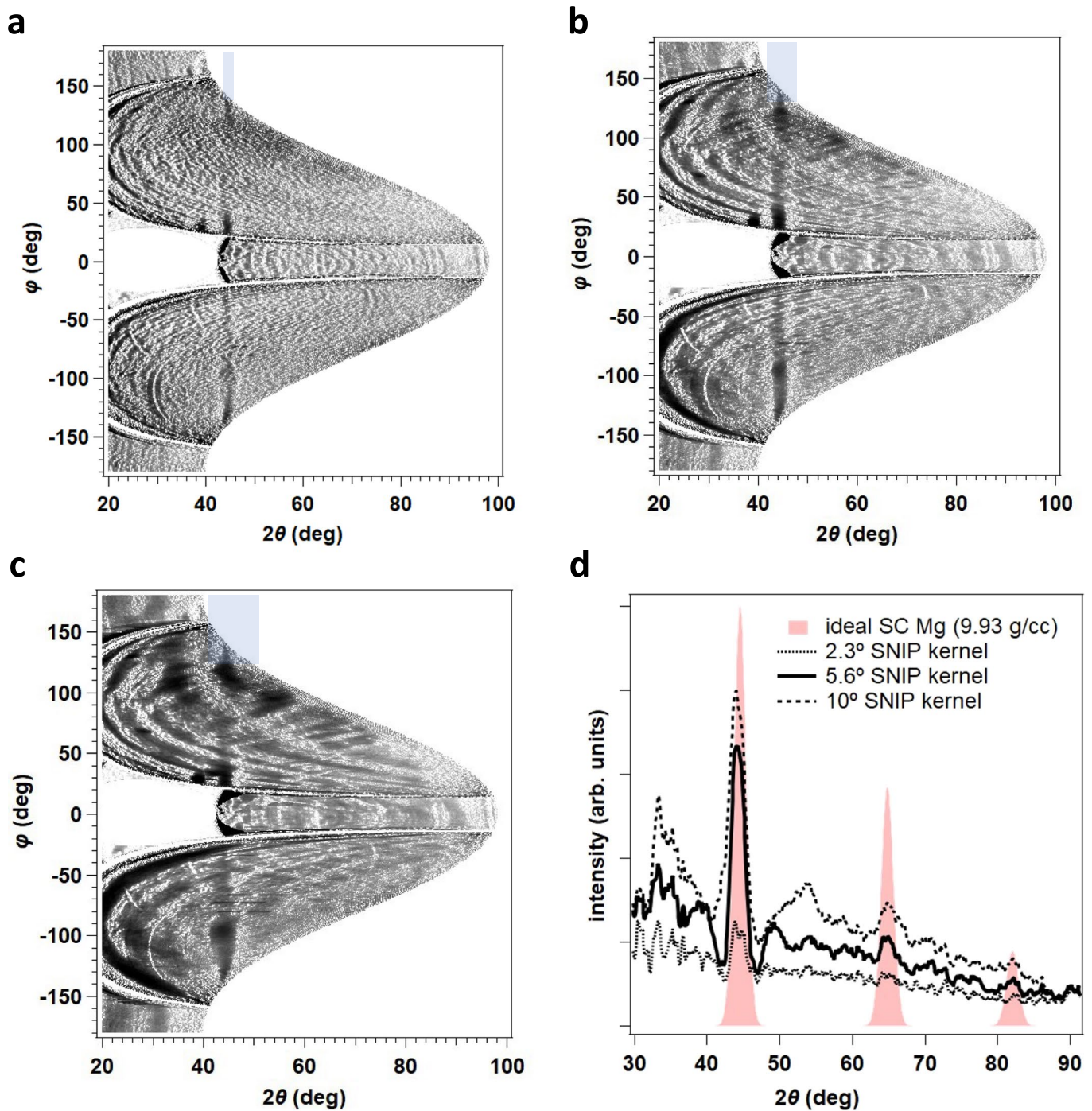
**Extended Data Fig. 2 | Summary of shot N170419-002 (0.56 TPa).** Raw image plate data are warped into (a) stereographic and polar (b) projections. Background-subtracted stereographic data is shown in (c) and (d) shows a radiation-hydrodynamic simulation of this experiment, with colors corresponding to pressure. The interfaces between different materials in the sample are indicated with horizontal red lines and the timing of the x-ray source is bracketed with vertical red lines. All materials in the sample (diamond, Re, Au, Be and Mg) may scatter x-rays onto the image plates during the time between  $\sim 24.2$  and  $26.2$  ns. (e) shows the background-subtracted polar projection. Everything within the red contours, which outline spurious features, and outside of the green contours, which encompass the region of interest on the image plates, is masked out to produce the image in the inset. An average lineout of the masked data is shown in the lower panel. The relative intensities of the Mg and Be simulated data are determined based on the relative thicknesses and scattering factors of these two target layers. Diffraction from Au was observed on shot N170209-003 but not on this shot, most likely because the Au layer (as well as the adjacent thin layer of Re) are predicted to be melted for this higher-pressure drive. On shot N170209-003 the pushers layer adjacent to the Mg sample was made of diamond, but on this shot is a layer of Be. Because of the larger volume of Be, and because about 1/3 of it is shielded from preheating by the Re/Au heat shield, it is reasonable to expect some beryllium scattering. The simulated pattern for ideal bcc Be is shown overlaid on the average data lineout in the lower panel of (e), with intensity scaled by the relative scattering factors and thicknesses of the two layers. The strongest Be line overlaps an Mg Fmmm line, so the presence of Be data in the diffraction pattern cannot be positively confirmed. As in shot N170209-003, there are several Laue spots from single-crystal diamond, outlined in red circles in (c), and powder-like diamond peaks with very strong preferred orientation, indicated in (e) using yellow arrows. The diffraction data and simulation (d) indicates that the bulk of the diamond window is in two distinct pressure states: About half is at pressure equilibrium with the sample and about half is at a lower pressure, as a release wave travels back into the window after the diamond elastic wave reaches the free surface. The upper image plate is shielded by 10  $\mu\text{m}$  of Ge and the s plate with 15  $\mu\text{m}$  of Ge, which strongly attenuate the helium-beta emission line in Ge XRS spectrum at 12.1 keV. The lower image plate has no Ge shielding however so, for the strongest diffraction signals, a second, weaker reflection is observed at lower angle. The clearest example is labeled for one of the diamond reflections in (e). Because the bottom image plate data is impacted by the presence of multiple diamond peaks and multiple emission lines, and because the background-subtraction tends to attenuate the Mg signal in the immediate vicinity of these strong diamond features, the lineout of the masked data reported in the lower panel of (e) is over the upper image plate only in region enclosed between the blue horizontal lines in the inset of (e). A feature worth noting on this shot is the linear drop in signal level outlined with the green dashed contour, corresponding to a crack or flaw in the Ge+polycarbonate image plate shielding. In the region next to the crack, there is an area with very high background and a small spot in which the image plate is saturated (purple arrow).



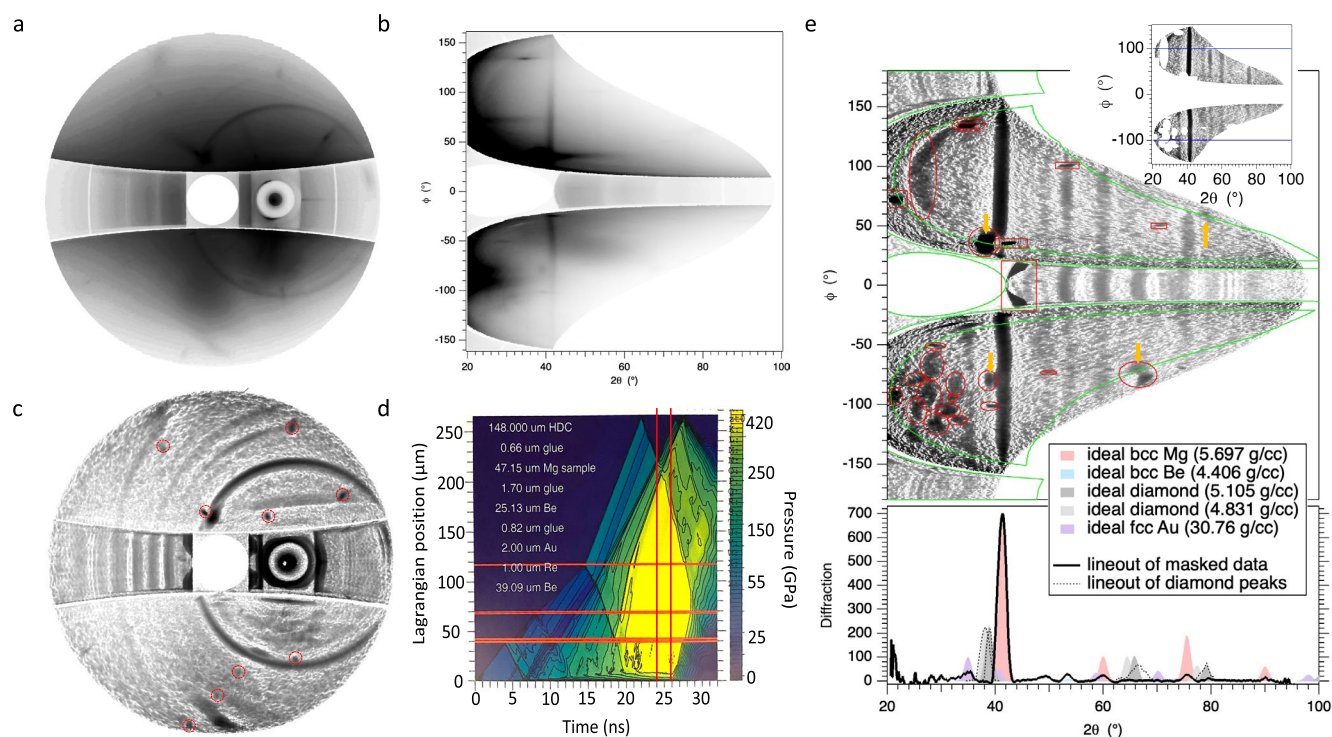
**Extended Data Fig. 3 | Summary of shot N171128-001 (0.96 TPa).** Raw image plate data are warped into stereographic (a) and polar (b) projections. Background-subtracted stereographic data is shown in (c) and (d) shows a radiation-hydrodynamic simulation of this experiment, with colors corresponding to pressure. The interfaces between different materials in the sample are indicated with horizontal red lines and the timing of the x-ray source is bracketed with vertical red lines. All materials in the sample (diamond, Re, Au, Be and Mg) may scatter x-rays onto the image plates during the time between ~27 and 29 ns. (e) shows the background-subtracted polar projection. Everything within the red contours, which outline spurious features, is masked out to produce the image in the inset. There was a scanning error that impacted the data on the rind image plate so it also was masked out. An average lineout of the masked data is shown in the lower panel. The relative intensities of the Mg and Be simulated data are determined based on the relative thicknesses and scattering factors of these two target layers. There are several Laue spots from single-crystal diamond, outlined in red circles in (c), and powder-like diamond peaks with very strong preferred orientation, indicated in (e) using yellow arrows. The diffraction data and simulation (d) indicates that the diamond window is in a range of pressure states: the majority appears to be at pressure equilibrium with the sample, but several of the peaks are smeared out to lower angles, consistent with releasing material closest to the free surface. A weak diffraction line is evident at  $\sim 74^\circ$ . We do not believe this weak diffraction line originated from the Mg sample as the intensity of the line is not uniform in azimuthal angle like the other Mg diffraction lines in this experiment or any of the other experiments in this study. As shown in Fig. S1, the starting ambient pressure Mg sample had very good powder averaging, and this expected to persist as the sample undergoes several transformations under pressure. This diffraction line has several bright, localized spots along the azimuth which are not consistent from originating from the Mg sample. Furthermore, the two-theta location of the line matches that of the high-pressure Bragg spot from the compressed diamond window. This line could therefore also originate from the high-pressure region of the diamond window. While single crystal diamond windows have been shown to retain their single crystallinity under ramp compression<sup>35</sup>, the possibility of small fraction of the diamond single crystal breaking up and thus contributing to the diffraction signal at different azimuthal angles cannot be ruled out.



**Extended Data Fig. 4 | Summary of shot N180301-001 (1.32 TPa).** Raw image plate data warped into stereographic (a) and polar (b) projections. Background-subtracted stereographic data is shown in (c) and (d) shows a radiation-hydrodynamic simulation of this experiment, with colors corresponding to pressure. The interfaces between different materials in the sample are indicated with horizontal red lines and the timing of the x-ray source is bracketed with vertical red lines. All materials in the sample (diamond, Re, Au, Be and Mg) may scatter x-rays onto the image plates during the time between ~27 and 29 ns. (e) shows the background-subtracted polar projection. Everything within the red contours, which outline spurious features, and outside of the green contours, which encompass the region of interest on the image plates, is masked out to produce the image in the inset. The data on the rind image plate was very noisy, with a large number of artefacts. A few of these are indicated in (c) with blue dashed lines. These appear after applying the background-subtraction to stitched image plate data. On high-background shots such as this, each image plate is scanned dozens of times to de-saturate it, and a final image is created by stitching together the most intense unsaturated regions of each subsequent scan. On the rind image plate, the background (and the gradient in the background) is extremely high so final image is composed of many stitched scans and there are therefore many closely-spaced artefacts, which make it difficult to mask the data and discriminate the diffraction data, so this image plate is masked out of the lineout in the lower panel of (e). There are a few possible Laue spots on this shot, circled in red in (c), and powder-like diamond peaks with very strong preferred orientation, indicated in (e) using yellow arrows. A beryllium ablator and window are used on this shot so we simulated the ideal diffraction pattern for bcc Be at about 1317 GPa, with the relative intensities of the Mg and Be modeled based on the relative thicknesses and scattering factors of these two target layers. The strongest Be peak lies at 62.6 degrees, and the relative intensity is so low that it does not rise above the background. The diffraction data and simulation (d) indicates that the bulk of the diamond window is in two distinct pressure states: About half is at pressure equilibrium with the sample and about a third is at a lower pressure, as a release wave travels back into the window after the diamond elastic wave reaches the free surface. The higher-pressure diamond peak at 44 degrees lies almost exactly on top of the low-angle simple cubic Mg peak, but its distinctive texture makes it easy to distinguish from very powder-like Be diffraction. There is an unusual diffuse background feature on the top image plate, outlined with a yellow dashed line in (a), that adds many strong artefacts after background-subtraction which are difficult to fully mask out. As a result, we have not extended the average lineout, taken between the blue horizontal lines in the inset of (e), to the edge of the upper plate. One other feature that is particularly pronounced on this shot is the attenuation of the signal just adjacent to the strongest diffraction peak by the background-subtraction procedure. The average diffraction intensity appears to become negative in two troughs below and above the peak at 44 degrees.



**Extended Data Fig. 5 |** Diffraction data for shot N180301-001 (1.32 TPa) with various widths of SNIP background filter. As can be seen, the observation of the second Mg diffraction line at  $66^\circ$  is observed in the background subtracted image when a  $2.6^\circ$  (a),  $5.6^\circ$  (b) or  $10^\circ$  (c) SNIP kernel is chosen. The SNIP algorithm can produce artifacts in the diffraction data such as the intensity troughs on either side of the strongest diffraction peak at  $44^\circ$  (d).



**Extended Data Fig. 6 | Summary of shot N180620-001 (0.41 TPa).** Raw image plate data warped into stereographic (a) and polar (b) projections. Background-subtracted stereographic data is shown in (c) and (d) shows a radiation-hydrodynamic simulation of this experiment, with colors corresponding to pressure. The interfaces between different materials in the sample are indicated with horizontal red lines and the timing of the x-ray source is bracketed with vertical red lines. All materials in the sample (diamond, Re, Au, Be and Mg) may scatter x-rays onto the image plates during the time between 24 and 26 ns. (e) shows the background-subtracted polar projection. Everything within the red contours, which outline spurious features, and outside of the green contours, which encompass the region of interest on the image plates, is masked out to produce the image in the inset. The data on the rind image plate has several distinct shadows, likely related to imperfections in the Ge filter, so this image plate is masked out of the lineout in the lower panel of (e). There are several Laue spots on this shot, circled in red in (c), and powder-like diamond peaks with very strong preferred orientation, indicated in (e) using yellow arrows. In the lower panel of (e), the lineout of the masked data is compared to simulated ideal patterns of the best-fit component phases. The relative intensities of the Mg and Be modeled based on the relative thicknesses and scattering factors of these two target layers. Here we have only considered that the Be pusher is contributing to the scattering signal. The ablator may also contribute however, which would double the simulated intensity, in better agreement with the experimental observation. The diffraction data and simulation (d) indicate that the bulk of the diamond window is in two distinct pressure states: About half is at pressure equilibrium with the sample and about a third is at a lower pressure, as a release wave travels back into the window after the diamond elastic wave reaches the free surface. There is a low-angle peak near 37 degrees that could be consistent with fcc Au. However, it is also at the right angle and relative intensity to be a secondary reflection of the most intense, lowest-angle Mg diffraction line, produced from Ge helium-beta (12.1 keV) x-rays. No Ge k-edge filter was used on the lower image plate in this shot, so the He-b line is not attenuated. This is a more likely peak identification, considering that this line is not clearly evident on the upper plate. On this shot only of all Mg experiments, the Ge XRS foil was driven from only one side rather than two, decreasing the effective source size and increasing the angular resolution of the diffraction data, and decreasing the total number of photons in the source. There is one clearly-evident peak near 49 degrees on this shot which is not described by any of the known or predicted phases present in the target, suggesting, as was the case for N170209-003, that the Mg is in a bcc-like distorted phase.

Shot	ablator	Heat shield	pusher	sample	tamper
N170209	Be [38.3 $\mu\text{m}$ ]	Au [2.2 $\mu\text{m}$ ]	{110}-orientation single crystal diamond [40 $\mu\text{m}$ ]	Mg rolled foil [46.5 $\mu\text{m}$ ]	{110}-orientation single crystal diamond [154 $\mu\text{m}$ ]
N170419	Be [39.7 $\mu\text{m}$ ]	Re [1.1 $\mu\text{m}$ + Au [1.2 $\mu\text{m}$ ]	Be [24.8 $\mu\text{m}$ ]	Mg rolled foil [46.5 $\mu\text{m}$ ]	{110}-orientation single crystal diamond [148 $\mu\text{m}$ ]
N171128	Be [37/5 $\mu\text{m}$ ]	Re [1 $\mu\text{m}$ ] + Au [1.8 $\mu\text{m}$ ]	Be [27.2 $\mu\text{m}$ ]	Mg rolled foil [48.0 $\mu\text{m}$ ]	{110}-orientation single crystal diamond [197 $\mu\text{m}$ ]
N180301	Be [39.4 $\mu\text{m}$ ]	Re [0.8 $\mu\text{m}$ ] +Au [1.9 $\mu\text{m}$ ]	Be [21.2 $\mu\text{m}$ ]	Mg rolled foil [46.3 $\mu\text{m}$ ]	{110}-orientation single crystal diamond [197 $\mu\text{m}$ ]
N180620	Be [39.1 $\mu\text{m}$ ]	Re [1.0 $\mu\text{m}$ ] +Au [1.8 $\mu\text{m}$ ]	Be [25.1 $\mu\text{m}$ ]	Mg rolled foil [47.2 $\mu\text{m}$ ]	{110}-orientation single crystal diamond [148 $\mu\text{m}$ ]

**Extended Data Table 1** | Summary of target materials and thicknesses for each experiment.

	N170209-003	N180620-001	N170419-002		N171128-001		N180301-001	
<b>Mg Stress (GPa)</b>	309 (-15, +52)	409 (-17, +53)	563 (-22, +54)		959 (-14, +64)		1317 (-49, +70)	
<b>Histogram Width (GPa)</b>	6	19	8		29		11	
<b>Mg phase</b>	d-bcc	d-bcc	<i>Fmmm</i>		sh		sc	
<b>Mg <math>2\theta_1</math> (°)</b>	27.90 (0.20)	41.28 (0.20)	(111)	42.21 (0.20)	(001)	42.82 (0.20)	(100)	44.26 (0.20)
<b>Mg <math>2\theta_2</math> (°)</b>	39.85 (0.20)	59.87 (0.22)	(020)	49.26 (0.20)	(010)	43.94 (0.20)	(110)	64.85 (0.24)
<b>Mg <math>2\theta_3</math> (°)</b>	49.51 (0.27)	75.56 (0.21)	(200)	55.81 (0.20)	(011)	63.79 (0.20)		
<b>Mg <math>2\theta_4</math> (°)</b>	57.96 (0.21)		(022)	66.81 (0.33)				
<b>Mg <math>2\theta_5</math> (°)</b>	65.08 (0.24)		(202)	72.67 (0.23)				
<b>Mg <math>2\theta_6</math> (°)</b>	72.80 (0.21)							
<b><i>a</i> (Å)</b>			2.583 (0.008)		1.866 (0.009)		1.596 (0.008)	
<b><i>b</i> (Å)</b>			2.906 (0.09)					
<b><i>c</i> (Å)</b>			3.346 (0.011)		1.628 (0.01)			
<b>density (g/cm<sup>3</sup>)</b>			6.427 (0.066)		8.221 (0.137)		9.930 (0.149)	

**Extended Data Table 2** | Summary of Mg diffraction data for each experiment.